mathematics

Article

An Improved Rock Damage Characterization Method Based on the Shortest Travel Time Optimization with Active Acoustic Testing

Jing Zhou [1,2], Lang Liu [1,2,*], Yuan Zhao [3], Mengbo Zhu [1,2], Ruofan Wang [1,2] and Dengdeng Zhuang [1,2]

[1] Energy School, Xi'an University of Science and Technology, Xi'an 710054, China; jingzhou@xust.edu.cn (J.Z.); mengbo_zhu@163.com (M.Z.); ruofan.wang@xust.edu.cn (R.W.); zddeng@126.com (D.Z.)
[2] Key Laboratory of Western Mines and Hazards Prevention, Ministry of Education of China, Xi'an 710054, China
[3] Department of Civil Engineering, School of Human Settlements and Civil Engineering, Xi'an Jiaotong University, Xi'an 712000, China; zhaoyuan92@xjtu.edu.cn
* Correspondence: liulang@xust.edu.cn

Abstract: Real-time evaluation of the damage location and level of rock mass is essential for preventing underground engineering disasters. However, the heterogeneity of rock mass, which results from the presence of layered rock media, faults, and pores, makes it difficult to characterize the damage evolution accurately in real time. To address this issue, an improved method for rock damage characterization is proposed. This method optimizes the solution of the global shortest acoustic wave propagation path in the medium and verifies it with layered and defective media models. Based on this, the relationship between the inversion results of the wave velocity field and the distribution of rock damage is established, thereby achieving quantitative characterization of rock damage distribution and degree. Thus, the improved method is more suitable for heterogeneous rock media. Finally, the proposed method was used to characterize the damage distribution evolution process of rock media during uniaxial compression experiments. The obtained results were compared and analyzed with digital speckle patterns, and the influencing factors during the use of the proposed method are discussed.

Keywords: rock damage; non-destructive testing; inversion of wave velocity field; damage characterization

MSC: 74L10

check for updates

Citation: Zhou, J.; Liu, L.; Zhao, Y.; Zhu, M.; Wang, R.; Zhuang, D. An Improved Rock Damage Characterization Method Based on the Shortest Travel Time Optimization with Active Acoustic Testing. *Mathematics* **2024**, *12*, 161. https://doi.org/10.3390/math12010161

Academic Editor: Smirnov Nikolay Nikolaevich

Received: 4 December 2023
Revised: 21 December 2023
Accepted: 26 December 2023
Published: 4 January 2024

1. Introduction

Rock is the main supporting material in underground engineering [1–3], and its damage degree evolves with time under the action of external factors such as force [3–6] temperature [7–9], and water [10–12]. Real-time detection and characterization of rock damage location and damage level is the key to preventing underground disasters [13–15]. The commonly used non-destructive characterization methods for rock damage include image method and acoustic method [16,17]. The image method characterizes the damage of rocks by comparing and identifying the images of the rock before and after the damage change [18,19]. The image method relies on high-resolution image acquisition equipment and is limited by lighting conditions and viewing angles. The acoustic wave method mainly analyzes the damage by imaging changes in the velocity of acoustic waves propagating in rocks [20,21]. The characterization method based on acoustic waves has more advantages in revealing the location and mechanism of key fracture damage of rocks and the future development direction of cracks [22,23]. Many studies have been carried out based on this method [24].

The wave velocity of the medium, which is usually obtained from the linear relationship between the acoustic wave test propagation distance and propagation time [25,26], is often associated with the mechanical properties of the medium to analyze its damage changes [27,28]. Madhubabu [29] et al. used multiple linear regression analysis (MVRA) and artificial neural network (ANN) to predict the compressive strength and elastic modulus of carbonate rocks by measuring parameters such as ultrasonic wave velocity and porosity. Hanxin Chen [30] et al. established a nonlinear Lamb wave detection system, analyzed the obtained time domain waveform using fast Fourier transform (FFT), and studied the impact of two types of defects on the non-linear effects of Lamb waves. Umrao [31] et al. proposed an adaptive neural fuzzy inference system (ANFIS) to predict the strength and elastic modulus of sedimentary rocks by measuring P-wave velocity and porosity, considering their heterogeneity. Abbas et al. tested the parameters of ultrasonic wave velocity, amplitude, and energy of composite sand shale and evaluated the macroscopic deformation and crack propagation of the sample. Abbas [32] et al. evaluated the macroscopic deformation and crack propagation of the sample using parameters such as the ultrasonic wave velocity, amplitude, and energy of composite sand shale. Rodríguez [33] et al. analyzed the distribution of damage within rock specimens under diametral compression with P-wave velocity calculation.

The wave velocity field imaging of the medium can be achieved by using multiple acoustic sensors and multiple sets of arrival data, which enables a more accurate analysis of the damage distribution of the rock medium [34,35]. The time-domain inversion calculation of the wave velocity field consists of two interrelated parts: forward and inversion [36]. The forward calculation algorithm determines the propagation model of the acoustic wave in the wave velocity field and obtains the theoretical travel time. In the iterative calculation, the difference between the theoretical and measured travel time data is continuously corrected to obtain the final value [37]. Based on the basic theory used in the inversion calculation, it can be divided into two types: wave velocity field inversion based on ray theory and wave velocity field inversion based on wave theory [38]. Gorbatov [39] et al. calculated the P-wave velocity structure of the Kamchatka Peninsula in the Western Pacific using 5270 shallow- and medium-depth earthquakes recorded in 32 stations of the Russian Geophysical Service Regional Seismic Network. Goodfellow [40] et al. used active and passive ultrasonic methods to study the evolution of the attenuation characteristics of the sandstone sample during true triaxial deformation, calculated the wave velocity field during the stress process of the rock sample, and established a relationship between the wave velocity field and the damage. Caibin Xu et al. [41] pointed out that the scattering behavior between Lamb waves and defects is closely related to wavelength and defect size. They proposed a multi-narrowband fusion method that utilizes Lamb wave information contained in multiple frequency bands to improve the image quality of Lamb wave phased array imaging.

The previous studies indicate that the key to real-time characterization of rock damage based on active acoustic testing is to establish the relationship between wave velocity field imaging results and damage. The shooting method (angle increment method) and bending method are the most basic local forward modeling methods [42], which have high computational efficiency but limited solution accuracy when the ray coverage density is insufficient. The global algorithm has a slower calculation speed but yields a more refined result of inverting the wave velocity field. The presence of layers, holes, and fissures in rock increases the difficulty of characterizing its damage. When the acoustic waves encounter various defects such as faults and holes in the medium, they change their paths. The received waveform information reflects such defect information of the medium [43,44]. Therefore, the rock damage distribution can be characterized by association with the wave velocity field of the rock. The challenge is how to solve the rock wave velocity field accurately and quickly.

An improved method for rock damage characterization based on the shortest travel time optimization with active acoustic testing is proposed. In Section 2, the global shortest travel time optimization based on Bellman–Ford is introduced to solve the distribution of the medium wave velocity field. Then, the connection between the wave velocity field and the rock damage distribution is established. In Section 3, a rock uniaxial compression experiment is used to verify the accuracy of the proposed method in characterizing the evolution of the damage distribution. In Section 4, the influence of emission waveform parameters on the results of the rock damage characterization method based on acoustic wave testing is discussed.

2. Method

2.1. Shortest Path Solution Based on Bellman–Ford Method

The Bellman–Ford algorithm, employed in dynamic programming, excels at finding the shortest path from a single source. Its integration into wave velocity field solutions swiftly yields the globally shortest travel time path, with a key emphasis on efficient relaxation calculations.

Figure 1 is an example of the Bellman–Ford algorithm finding the shortest path from S. Figure 1 illustrates the nodes along the propagation paths and the corresponding propagation times for each sub-path. The initial propagation time is 0. The initial slack involves comparing the propagation paths to all adjacent nodes to identify the shortest propagation time path. Given that $t_1 < t_5$, the shortest path is S-R_1, with a recorded shortest path travel time of 1. In the second slack calculation, considering $t_1 + t_2 < t_5$, the shortest path is revised to S-R_1-R_2, and the recorded shortest travel time is updated to 3. In the third slack calculation, $t_1 + t_2 + t_3 < t_5$ results in the shortest path being S-R_1-R_2-R_3, with a recorded shortest path travel time of 5. Finally, considering $t_1 + t_2 + t_3 + t_4 < t_5$, the fourth slack calculation yields the shortest path as S-R_1-R_2-R_3-R. The steps above can calculate the shortest travel time path from S to R.

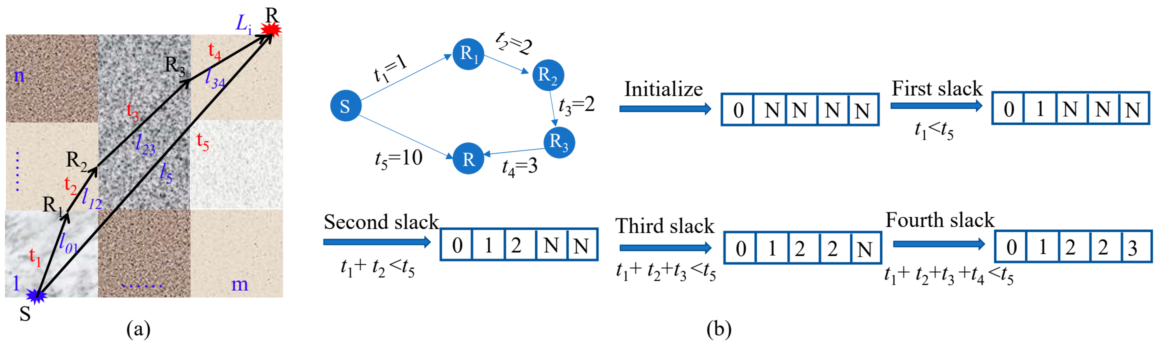

Figure 1. The principle of the shortest path calculation using the Bellman–Ford algorithm. (**a**) is a schematic diagram of the straight line propagation path and the refraction propagation path. (**b**) is the Bellman Ford algorithm to calculate the shortest propagation path considering refraction.

The shortest travel time path algorithm can obtain a path that adheres to Snell's law. It can quickly find the globally shortest path from multiple start nodes to multiple termination nodes. It has more advantages in the wave velocity field calculation of rock materials than the ray tracing method.

We thus used the Bellman–Ford algorithm to solve the shortest travel time path and analyze several common models' global acoustic wave propagation paths in rock damage characterization.

Figure 2a shows a homogeneous medium with a wave velocity of 3000 m/s and 12 sensors. These sensors can transmit and receive acoustic waves. The shortest path solution method based on the Bellman–Ford algorithm obtains the shortest propagation time path in the whole field. The results of the propagation path with the shortest time are shown in Figure 2a. In homogeneous media, the theoretical propagation path with the shortest time is the linear distance between the emission point and the reception point. The solved propagation path with the shortest time conforms to the theoretical results.

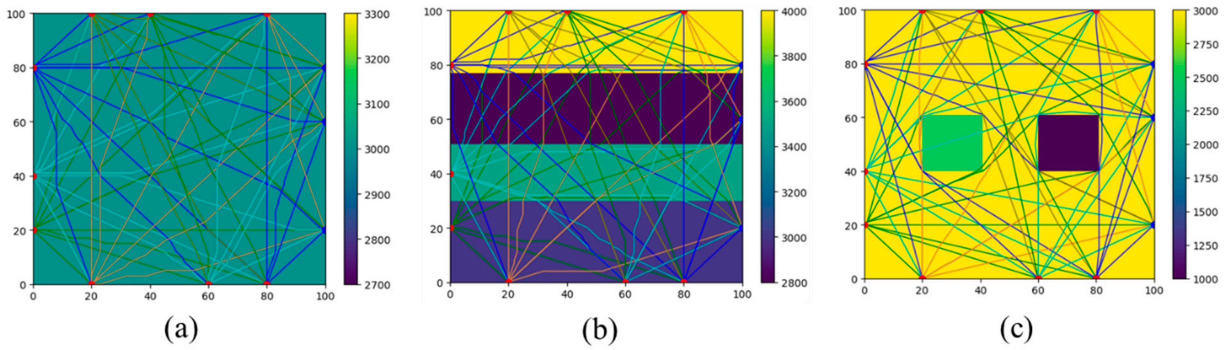

Figure 2. Propagation path with the shortest time of several common models obtained by the Bellman–Ford algorithm. (**a**–**c**) are the propagation path diagrams of the improved algorithm in homogeneous media, layered media and defective media respectively.

Figure 2b shows a layered medium with velocities of 4000 m/s, 2800 m/s, 3500 m/s, and 3000 m/s from top to bottom. The thickness from top to bottom is 24 m, 26 m, 20 m, and 30 m, respectively, and there are 12 sensors for acoustic testing. The propagation path with the shortest time obtained based on the Bellman–Ford algorithm is shown in Figure 2b. Results show that the acoustic wave propagation path refracts at the interface of the layered medium, which is consistent with the hypothetical situation.

Figure 2c shows a medium with a defect area. Its background wave velocity is 3000 m/s, including two defects with different wave velocities. The wave velocity of one defect area is 2500 m/s, which is slightly lower than the background wave velocity. The other is an ultra-low wave velocity zone, with a wave velocity of 1000 m/s.

According to Snell's law, acoustic waves preferentially propagate through areas with higher propagation speeds. Diffraction will occur in the area with ultra-low wave velocity. The propagation time with a straight line is the shortest one corresponding to the area, with little difference from the background wave velocity. The results in Figure 2 are also consistent.

2.2. Wave Velocity Field Calculation

Once the fastest propagation path is determined, the theoretical propagation time for each path is calculated under the assumed initial wave velocity background. This calculation uses the whole field's shortest propagation path solution method based on the Bellman–Ford algorithm. The medium's wave velocity model undergoes continuous refinement based on the arrival time of the received waveform. The wave velocity field of the medium is derived by minimizing errors. The Radon inverse transform is employed to iteratively establish an initial value for calculating the initial wave velocity field, mitigating the influence of the initial value on the calculation results.

As shown in Figure 1a, a medium is divided into m × n units, including several acoustic emission and receiving sensors. The path from one acoustic emission position to the acoustic receiving position is L_{i}, and its propagation sub-path in each small unit is l_{ij}. The corresponding time of each sub-path is t_{ij}, and the total propagation time is T_i.

The process of the acoustic signal from the acoustic emission point to the acoustic receiving position along the shortest travel time path is Radon positive transformation. The internal information of the inverse medium is the Radon inverse transform. According to Radon changes, the following is true:

$$t_i = \int\limits_{L_i} \frac{1}{v_j(x,y)} dl = \int\limits_{L_i} f_j(x,y) dl, \tag{1}$$

where $v_j(x,y)$ is the wave speed of the jth small unit, and $f_j(x,y)$ is the reciprocal of the jth small unit's wave speed.

When the wave velocity grid of the small element assumed for wave velocity inversion is small enough, the distance can be considered as a constant, and Equation (4) can be changed as follows:

$$t_i = \sum_{j=1}^{m} a_{ij} x_j, \tag{2}$$

$$\begin{cases} t_1 = a_{11}x_1 + a_{12}x_2 + \cdots + a_{1m}x_m \\ t_2 = a_{21}x_1 + a_{22}x_2 + \cdots + a_{2m}x_m \\ \vdots \\ t_n = a_{n1}x_1 + a_{n2}x_2 + \cdots + a_{nm}x_m \end{cases}, \tag{3}$$

where t is the monitored arrival time; a is the propagation length obtained by the Bellman–Ford algorithm; x is the slowness of wave velocity.

The back projection algorithm (BPT) is used to solve the problem. We can take the calculation of the wave velocity of cell j in Figure 1a as an example. The wave velocity of cell j is determined by dividing the cumulative time of all paths propagating in cell j by the cumulative path length propagating in cell j. The propagation time of each path in cell j is weighted by the ratio of the propagation path length l_{ij} of the ith acoustic propagation path in cell j to the total length L_i of the ith acoustic propagation path. The ith acoustic propagation path total travel time (T_i) is allocated to each small cell (t_i) of inverse wave velocity. The mathematical expression for solving wave velocity x_i of any grid is as follows:

$$x_i = \sum_{i=1}^{m} \left[T_i \left(\sum_{j=1}^{n} l_{ij} \middle/ L_i \right) \right] \bigg/ \sum_{i=1}^{m} l_{ij}. \tag{4}$$

This calculation result is taken as the initial value of the least squares iteration [45]. The error between theoretical travel time and monitoring travel time is illustrated as follows:

$$\begin{cases} \varepsilon_1 = t_1 - a_{11}x_1 + a_{12}x_2 + \cdots + a_{1m}x_m \\ \varepsilon_2 = t_2 - a_{21}x_1 + a_{22}x_2 + \cdots + a_{2m}x_m \\ \vdots \\ \varepsilon_m = t_n - a_{n1}x_1 + a_{n2}x_2 + \cdots + a_{nm}x_m \end{cases}. \tag{5}$$

Then, the sum of squared errors is as follows:

$$\varepsilon = \varepsilon_1^2 + \varepsilon_2^2 + \cdots + \varepsilon_n^2 \tag{6}$$

The slow derivation of each wave to be solved is as given:

$$\begin{cases} \frac{\partial \varepsilon}{\partial x_1} = 0 \\ \frac{\partial \varepsilon}{\partial x_1} = 0 \\ \vdots \\ \frac{\partial \varepsilon}{\partial x_m} = 0 \end{cases}. \tag{7}$$

Substituting into Equation (2), we obtain the following:

$$\begin{cases} -2\sum_{i=1}^{n} a_{i1}[t_i - (a_{11}x_1 + a_{12}x_2 + \cdots + a_{1m}x_m)] = 0 \\ -2\sum_{i=1}^{n} a_{im}[t_i - (a_{11}x_1 + a_{12}x_2 + \cdots + a_{1m}x_m)] = 0 \\ \vdots \\ -2\sum_{i=1}^{n} a_{im}[t_i - (a_{11}x_1 + a_{12}x_2 + \cdots + a_{1m}x_m)] = 0 \end{cases} \tag{8}$$

We can convert this to the following:

$$\begin{cases} \sum\limits_{i=1}^{n} a_{i1}(a_{11}x_1 + a_{12}x_2 + \cdots + a_{1m}x_m) = \sum\limits_{i=1}^{n} a_{i1}t_i \\ \sum\limits_{i=1}^{n} a_{i2}(a_{11}x_1 + a_{12}x_2 + \cdots + a_{1m}x_m) = \sum\limits_{i=1}^{n} a_{i2}t_i \\ \vdots \\ \sum\limits_{i=1}^{n} a_{im}(a_{11}x_1 + a_{12}x_2 + \cdots + a_{1m}x_m)] = \sum\limits_{i=1}^{n} a_{im}t_i \end{cases}. \tag{9}$$

Then, the wave velocity of each unit can be obtained as follows:

$$\boldsymbol{x} = \left[\boldsymbol{A}^T\boldsymbol{A}\right]^{-1}\boldsymbol{A}^T\boldsymbol{T} \tag{10}$$

2.3. Damage Distribution Calculation

In the study of rock damage characterization, the damage factor D used to describe the damage level of the medium is a variable related to the initial and final state of the medium, and its value is between 0 and 1. D is 0 when the rock is undamaged, and D is 1 when it is completely damaged.

Assume that the initial wave velocity before rock damage occurs is V_0, the wave velocity measured under the current damage degree is V_i, and the wave velocity when the rock completely loses its bearing capacity is V_c. The relationship between acoustic wave velocity and rock damage can be established as follows [46]:

$$D = 1 - (\frac{V_i}{V_c})^2. \tag{11}$$

In damage mechanics, strain is related to D as follows:

$$D = 1 - \exp[-a(\frac{\varepsilon_i}{\varepsilon_c})^b] \tag{12}$$

where ε_i is the current strain of the rock; ε_c is the strain when the rock is completely damaged.

Since the strain of the rock under load is positively correlated with the wave velocity, the functional relationship between the wave velocity change and the damage level is as follows:

$$D = 1 - \exp[-a(\frac{\Delta V_i}{\Delta V})^b], \tag{13}$$

where ΔV_i is the current wave velocity variation. ΔV is when the rock is completely damaged. Parameters a and b are set according to the range of wave velocity variation of the damaged rock mass.

Assuming the medium is completely damaged, its wave velocity decays to half its original value. The corresponding functional relationship between the damage and the measured wave velocity is shown in Figure 3.

Adjusting parameters a and b in Equation (13) can correct the sensitivity of wave velocity to characterize damage. When it is necessary to discern the minor damage, reduce a and increase b; when minor damage is not noticed, increase a and reduce b.

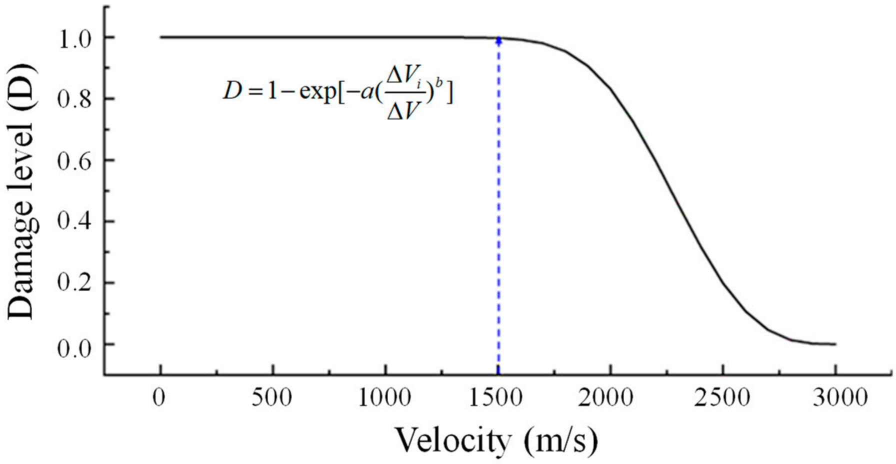

Figure 3. The corresponding functional relationship between the damage and the measured wave velocity.

2.4. Results

The improved method is used to calculate the wave velocity field distribution of the defective model in Figure 2c. The results are shown in Figure 4a. Figure 4b shows the wave velocity field distribution calculated by the initial method. The imaging unit error rate is shown in Figure 5. The newly improved method has slightly higher calculation accuracy than the initial method.

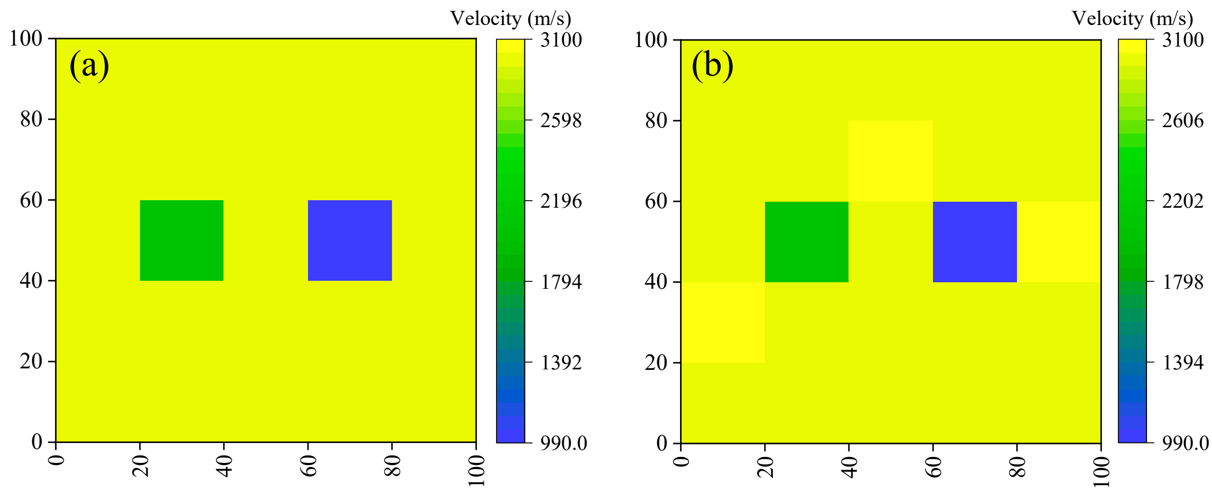

Figure 4. Results of the wave velocity field distribution: (**a**) is obtained by the improved method; (**b**) is obtained by the initial method.

In practical applications, the travel time data obtained from acoustic testing are used as observation values in wave velocity field inversion calculations. The disturbance analysis is of great significance. In the model shown in Figure 2c, a 1% travel time error disturbance is added to two, four, six, and eight paths. Then, the perturbed time shift data are used for wave velocity field inversion calculation. Figure 6 shows the error rate results for each calculation unit. The error rate gradually increases as the number of paths disturbed by travel time errors increases, and the error rate is lower for larger damage. The proposed method is still applicable when the number of paths with travel time error is less than six.

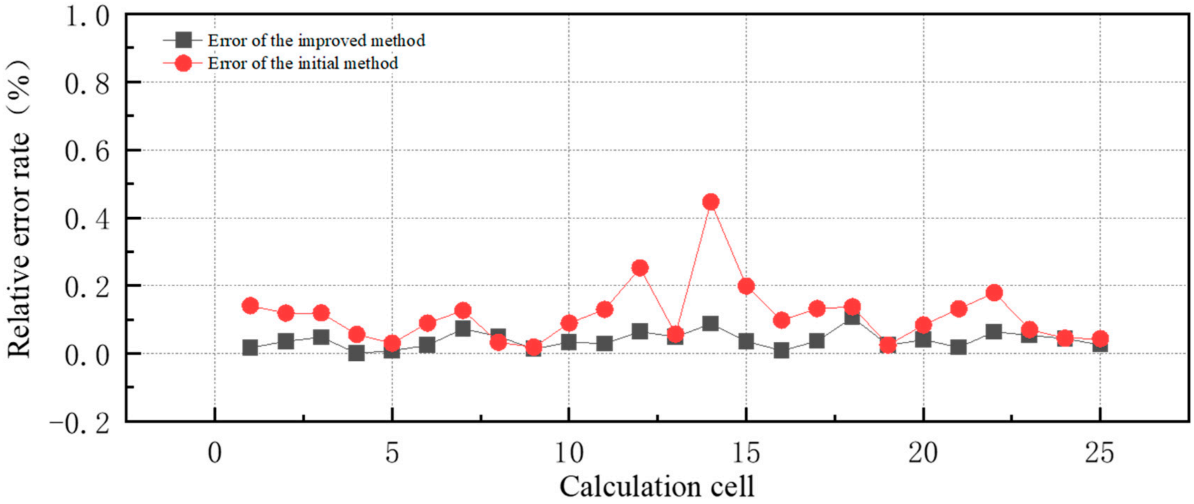

Figure 5. The relative error rate of all the calculation cells.

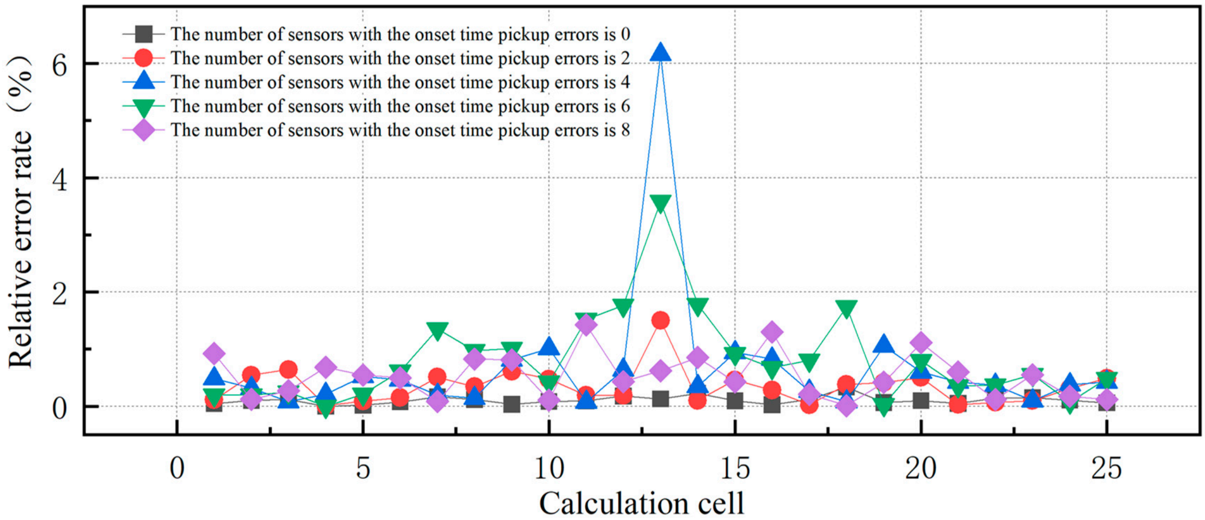

Figure 6. The relative error rate of each calculation unit when the number of measurement error paths is different.

3. Experimental Verification

3.1. Sample and Experiment

The equipment used in the experiment is shown in Figure 7. The uniaxial compression loading equipment provided external force to the rock sample to cause damage. The acoustic emission monitoring equipment was used to monitor the fracture signal of the rock damage process. Moreover, we utilized AST to test the current wave velocity of the rock sample at different stages. The industrial camera was used to take pictures of the damage process of rock samples.

The uniaxial compression equipment is an MTS-322T electro-hydraulic servo control testing machine from the Mechanical Testing Center of Central South University, with a load range of ±500 kN and a load accuracy of ±0.5%. The AE monitoring equipment is the DS5-16C AE acquisition system of Beijing Soft Island Times Technology Co., Ltd. (Beijing, China). It has 16 channels in total, and the range of its sampling frequency is 3 MHz–10 MHz. The matched AE amplifier is adjustable at 20/40/60 dB, and the model of the AE sensor is RS-2A. The industrial camera used in the experiment is the German Basler industrial camera (aca1920-155). Its highest sampling rate is 160 images per second, with a resolution of 5 million pixels.

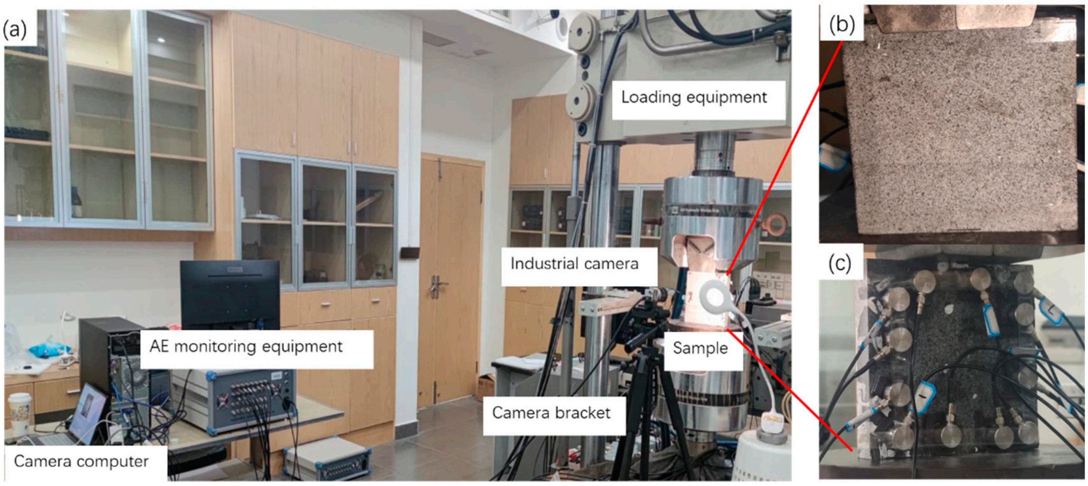

Figure 7. (**a**) is the experimental equipment and samples; (**b**) is one surface of the sample for industrial camera photography; (**c**) is the other surface of the sample for acoustic test and AE monitoring.

The flat granite sample with a side length of 150 mm and a thickness of 20 mm is shown in Figure 7b. The wave velocity of the complete sample is 3916 m/s, and the surface wave velocity is 2672 m/s. The photographing surface and the acoustic testing surface of the sample are shown in Figure 7b,c.

3.2. Experiment Process

The uniaxial compression test was conducted on the servo-hydraulic rock mechanics test system (MTS-322), with a loading rate of 5 kN/min.

Twelve sensors were arranged on the surface of the sample for acoustic testing. Table 1 displays the location coordinates of these sensors. The acoustic wave test transmitted the acoustic wave in turn on the acoustic test surface of the sample by calling the AST function in the DS5-16C AE acquisition system, and the excitation waveform used in the test was a pulse wave. First, an acoustic test was conducted before the experiment. Then, an acoustic test was conducted every 30 kN. Loading was stopped when the sample had visible cracks.

Table 1. Coordinates of the sensor.

	Sensors' Number											
	1	**2**	**3**	**4**	**5**	**6**	**7**	**8**	**9**	**10**	**11**	**12**
X	15	60	110	135	135	135	135	90	40	15	15	15
Y	15	15	15	15	60	110	135	135	135	120	90	50

The microfracture signal during uniaxial compression of the rock sample was monitored and collected by the AE monitoring system (DS5-16C), and the AE acquisition sensor was consistent with the acoustic testing sensor. The sampling frequency of the AE monitoring system is 3 MHz, and the signal amplification factor is 40 dB.

The Basler Aca1920-155 industrial camera took pictures of the sample deformation process during the experiment. The photographic surface of the industrial camera was opposite to the acoustic testing surface. The auxiliary white light source was used to illuminate the sample surface, improve brightness, and reduce the camera ISO parameters. The camera shooting resolution is 1920 $\times$ 1200 pixels, and the frame rate is 10 fps. These photos were processed by DIC technology. Since the granite sample has small, natural black and white units, and the size met the requirements, the sample surface did not require additional markings.

Figure 8a illustrates the change process of the loading force over time. Before the experiment, the wave velocity of the sample was measured once. Then, an acoustic test was carried out every 30 kN increase in load. After visible cracks appeared, the last acoustic test was carried out. A total of eight acoustic tests were carried out during the experiment. The time of each acoustic test is shown at the arrow positions in Figure 8a.

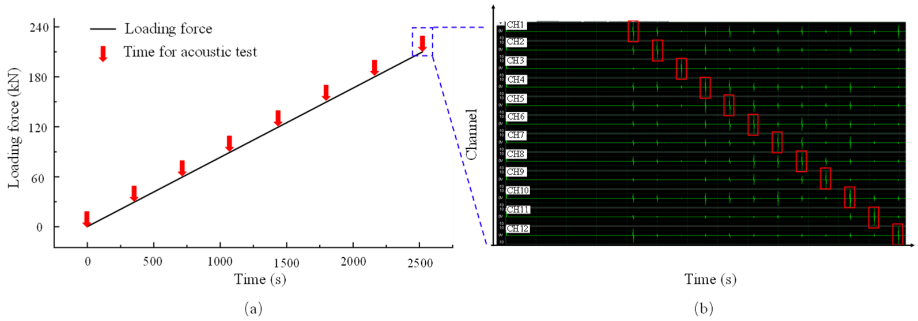

Figure 8. (**a**) The loading force changes with time and the time of the acoustic wave test; (**b**) is each channel's transmitted and received waveform. The red box is the excitation signal; the rest are the received signals.

The 12 sensors transmitted pulse waves in turn, and the others received acoustic waves propagating along the sample. The acoustic signals collected in the acoustic test are shown in Figure 8b. From top to bottom, they are the signals received by 12 channels. The red box is the excitation signal; the rest are the received signals.

Sensors at the ends were selected for analysis. The #2 sensor transmitted acoustic waves, and the #8 sensor received the waves propagating along the sample. The waveform received by the #8 sensor is shown in Figure 9.

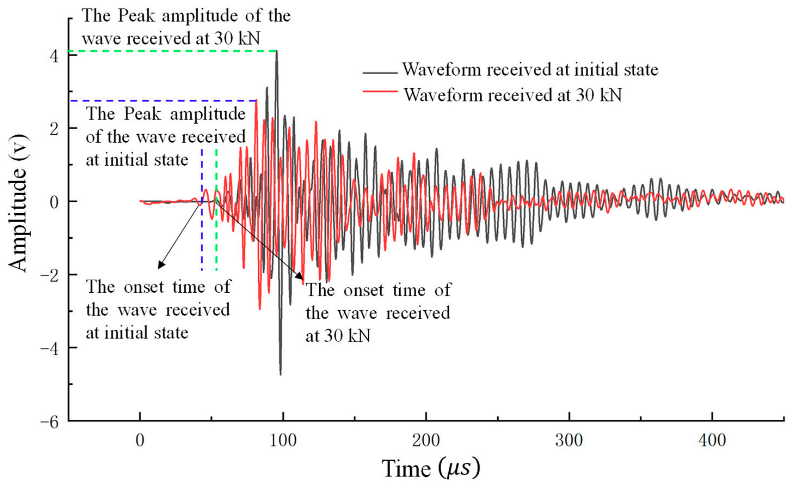

Figure 9. In the initial state and when the loading force is 30 kN, sensor 2 transmits acoustic waves, and sensor 8 receives waveforms.

3.3. Results

In this section, the damage location of the granite sample was characterized by calculating the change in the wave velocity field during the uniaxial compression test. The relationship between the wave velocity field and the damage was also established. The accuracy of the improved method to characterize the damage position was obtained by comparing the change results of the wave velocity field with the sample strain results calculated by DIC.

The size of the plate granite sample is 150 mm × 150 mm. Excluding the diameter of the acoustic emission sensor (18 mm), the size of the wave velocity calculated area in the plate sample is 120 mm × 120 mm. A total of 54 measuring paths could be made up of 12 sensors through the monitoring area. Utilizing the Bellman–Ford algorithm in dynamic programming, the initial velocity field of the plate granite sample was obtained by solving the shortest path within the calculated area. According to the relationship between wave velocity change and damage characterization established in Section 2.3, the damage of the sample during the loading process was characterized. The parameter range is generally set at 0.2~0.8 in rock uniaxial compression experiments. It can be calculated that a and b in Equations (2) and (3) are 3 and 6, respectively. The damage variable D is shown in Figure 10.

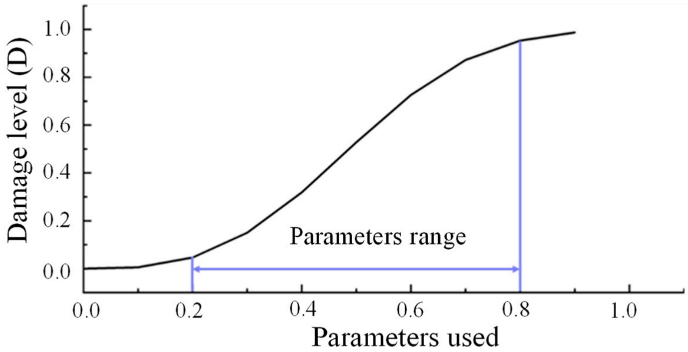

Figure 10. Parameter selection.

Figure 11 illustrates the wave velocity field distribution, damage distribution, and strain field of the rock sample during uniaxial compression. The damaged area identified by the improved method was consistent with the large strain area identified by the DIC technique.

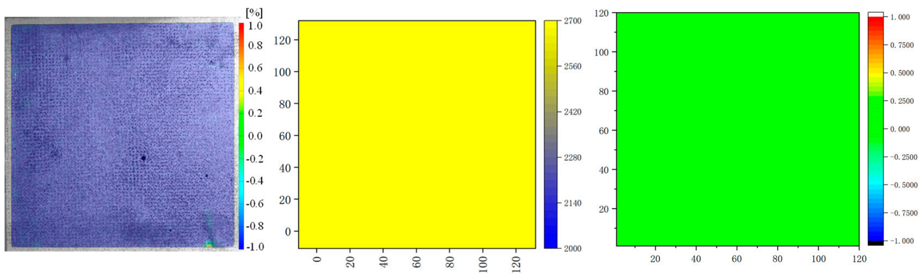

(**a**) Damage characterization results when the loading force is 30 kN.

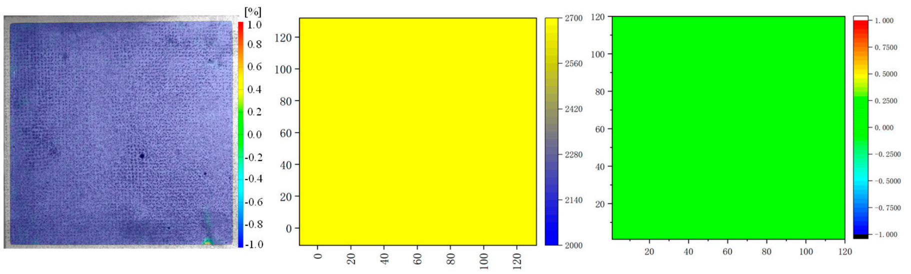

(**b**) Damage characterization results when the loading force is 60 kN.

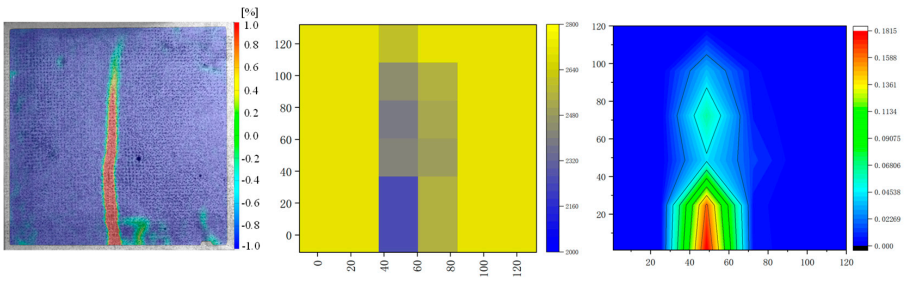

(**c**) Damage characterization results when the loading force is 90 kN.

Figure 11. *Cont.*

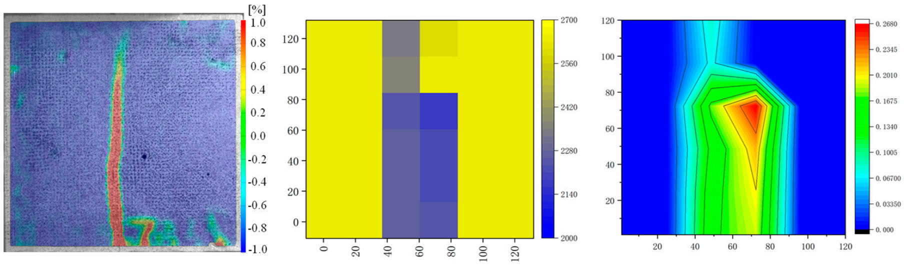

(**d**) Damage characterization results when the loading force is 120 kN.

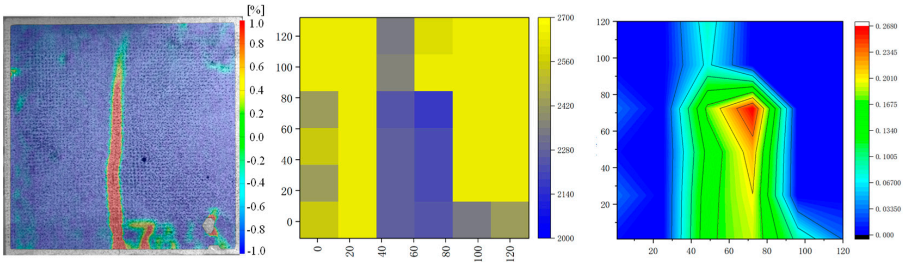

(**e**) Damage characterization results when the loading force is 150 kN.

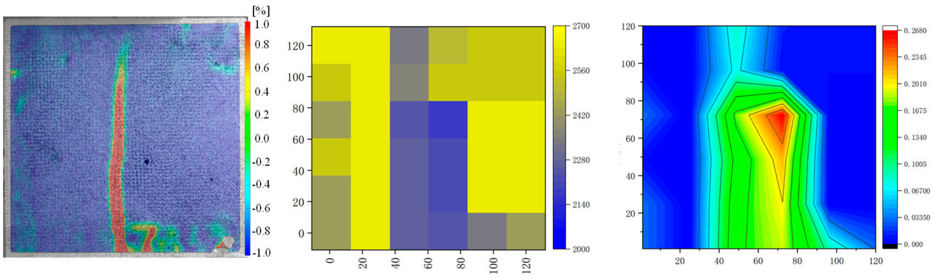

(**f**) Damage characterization results when the loading force is 180 kN.

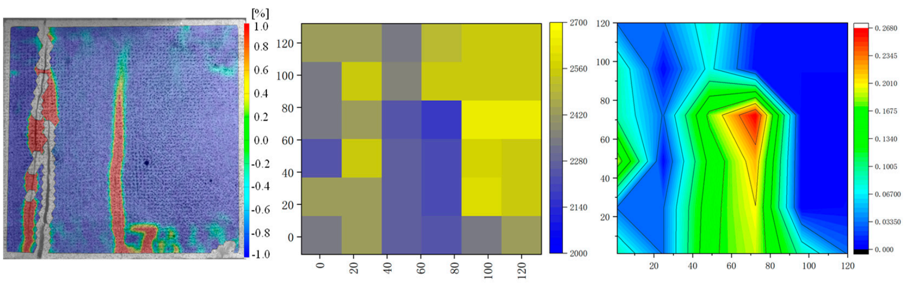

(**g**) Damage characterization results when the loading force is 210 kN.

Figure 11. Damage characterization results and digital speckle results with different loading forces.

4. Discussion

4.1. Sample and Experiment

The method presented in this paper provides a concise and accurate method for characterizing the damage distribution of rock. In practical applications, the degree of damage increases the internal cracks within the rock. It is thus necessary to analyze the influence of cracks on the acoustic testing method. This section analyzes the influence of waveform type, waveform parameters, and the relative position of a transmitted waveform and defect on the received waveform by the experiment.

The sample used was a granite slab sample with a crack in the center, as shown in Figures 5–10. Its size is 150 mm × 150 mm × 20 mm. The crack is at the center of the sample, as shown in Figure 12. The crack length is 20 mm, and the width is 2 mm.

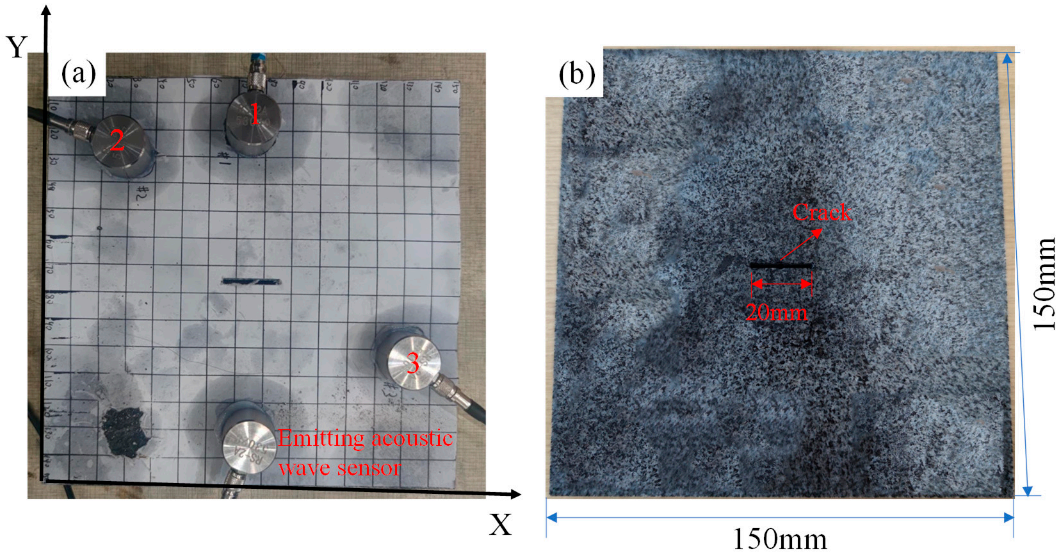

Figure 12. The granite slab sample with a crack. (**a**) is the relative position of the sensor and the crack on the flat sample; (**b**) is the size of the crack and the granite slab sample.

The AE equipment can emit the waveform edited by the user and collect the waveform transmitted through the sample. As shown in Figure 12, four AE sensors were arranged on the sample: one transmitting acoustic wave sensor and the other three receiving acoustic wave sensors. The sensor coordinates are shown in the Table 2.

Table 2. Sensor coordinates.

		AE Location	Sensor #1	Sensor #2	Sensor #3
Coordinates	X	75	75	30	130
	Y	20	130	120.4	50

The straight-line distances between the transmitting acoustic wave sensor and the three receiving acoustic wave sensors were 110 mm, 110.02 mm, and 62.65 mm, respectively. Compared with the position of the crack, the No. 1 sensor and the emitting acoustic wave sensor were located on both sides of the crack, and a straight-line distance passed through the crack. The No. 2 and emitting acoustic wave sensors were located on both sides of the crack, respectively, but the straight-line distance did not pass through the crack. The No. 3 sensor and the transmitting acoustic wave sensor were located on one side of the crack, and the straight-line distance did not pass through the crack.

The influence of the emitted sound wave frequency, different waveforms, and the relative position of the waveform and the defect on the received waveform was studied using this sample.

4.2. The Influence of Transmitting Acoustic Wave Frequency on Receiving Waveform Parameters

When studying the influence of the transmitted acoustic wave frequency on the received waveform, we chose sensor #3 for analysis because it could avoid the influence of cracks on the arrival of the first break. The emitting wave was a half-cycle sine wave with frequencies of 200 kHz, 400 kHz, 600 kHz, 800 kHz, and 1 MHz, respectively. The amplitude of the waveform was 1 V. The duration of the waveform was 2.5, 1.25, 0.833, 0.625, and 0.5, respectively, as shown in Figure 13.

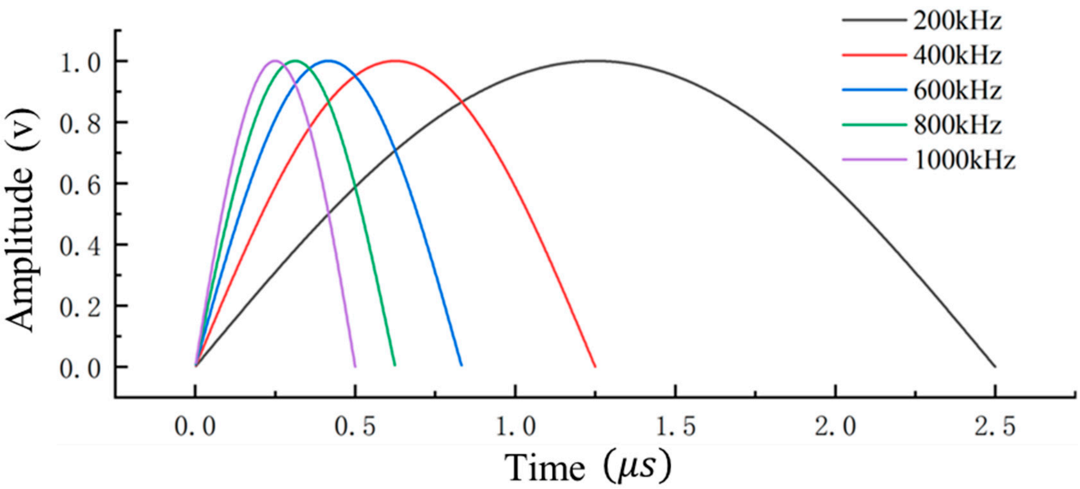

Figure 13. The emitting wave with frequencies of 200 kHz, 400 kHz, 600 kHz, 800 kHz, and 1 MHz, respectively.

We analyzed the waveform received by sensor #3. In Figure 14, (1) to (5) are the spectrum analysis results of the waveform received by sensor #3 when the transmitted waveform was 200 kHz, 400 kHz, 600 kHz, 800 kHz, and 1 MHz.

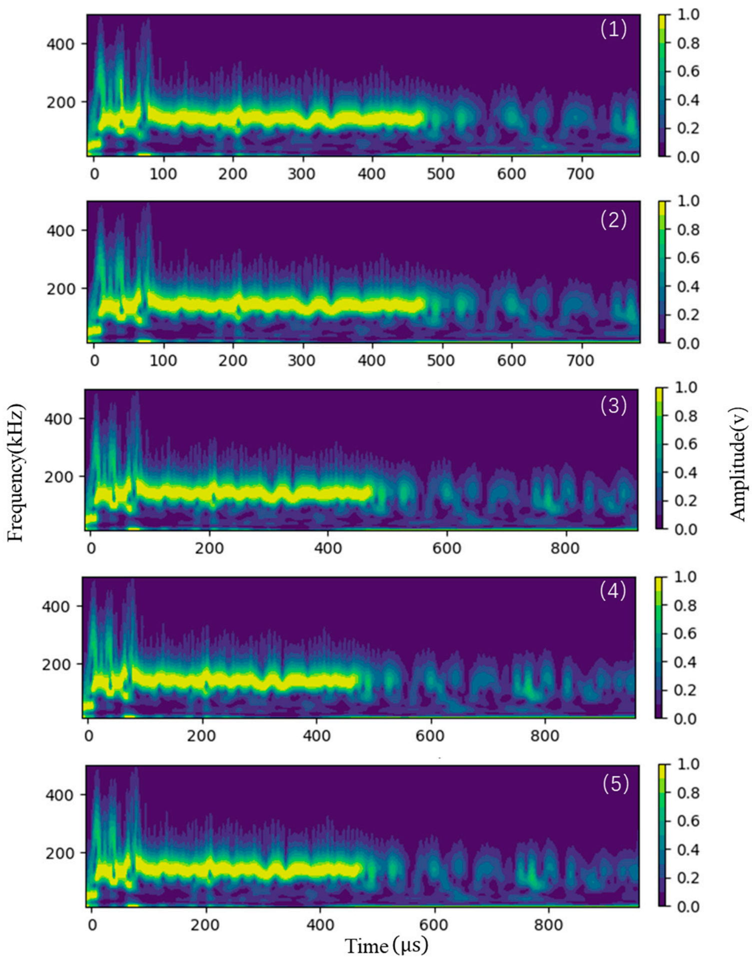

Figure 14. The spectrum analysis results of the waveform received by sensor #3. (**1**)–(**5**) are the spectrum analysis results of the waveform received by sensor #3 when the transmitted waveform was 200 kHz, 400 kHz, 600 kHz, 800 kHz, and 1 MHz.

The onset time, amplitude, and correlation coefficient of the received waveform were obtained for analysis. The correlation coefficient was based on the waveform received at 200 kHz, and the other received waveforms and their correlation coefficients were calculated, respectively. The results are shown in Table 3.

Table 3. The parameters of receiving waveform.

	Frequency of the Emitting Waveform				
	200 kHz	**400 kHz**	**600 kHz**	**800 kHz**	**1000 kHz**
Onset time (μs)	23.7	23.3	23.3	23.3	23.7
Amplitude (mV)	140.2	139.77	139.16	138.86	138.24
Correlation coefficient	1	0.98	0.97	0.97	0.96

The difference between the obtained parameters is small. The correlation coefficient of the oscillation start time and the waveform does not exhibit a clear change law. Although the amplitude changes are small, they gradually decrease with the frequency increase. That is, the higher the waveform frequency, the faster the attenuation.

4.3. Influence of Different Waveforms on Parameters of Received Waveforms

The half-cycle sine wave, rectangular wave, and triangular wave with a frequency of 1 MHz were used to study the influence of different transmitting waveforms on the parameters of the receiving waveform. The transmitted waveforms are shown in Figure 15; their amplitude was 1 V, and the duration was 0.5 μs.

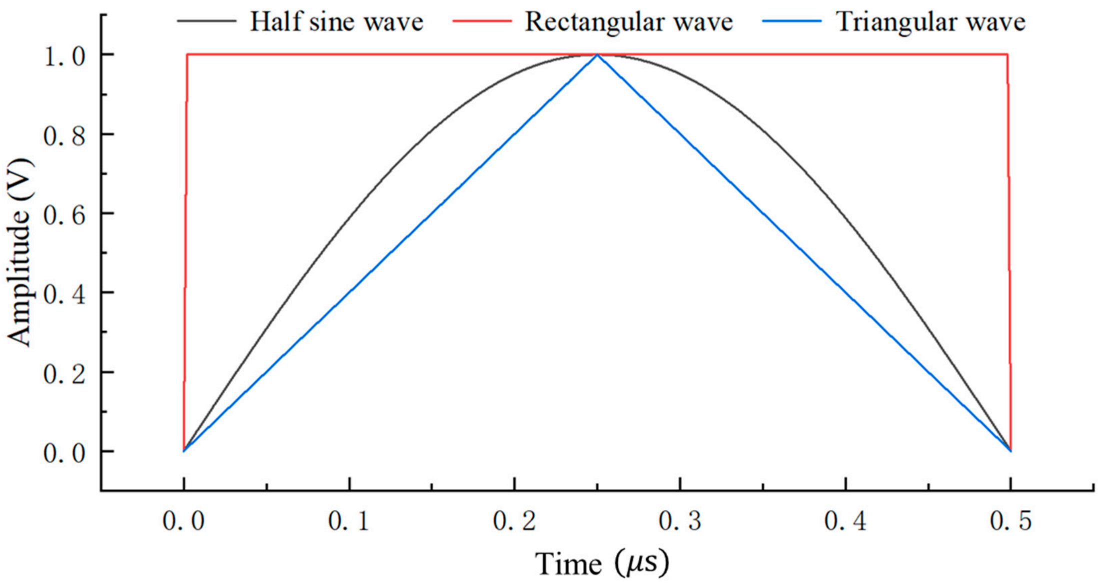

Figure 15. The different emitting waveforms.

We analyzed the waveform received by the No. 3 sensor. The spectrum analysis results of the receiving waveform are shown in Figure 16. The onset time, peak amplitude, and time of peak amplitude are shown in Table 4. The results show that the different types of waveforms do not affect the onset time and the time when the peak amplitude appears. But it does affect the magnitude. For waveforms of the same frequency, the peak amplitude of the rectangular wave is the largest, and the peak amplitude of the sine wave is the smallest. In practical applications, the transmission waveform is rectangular, which is more conducive to the propagation of the excitation waveform.

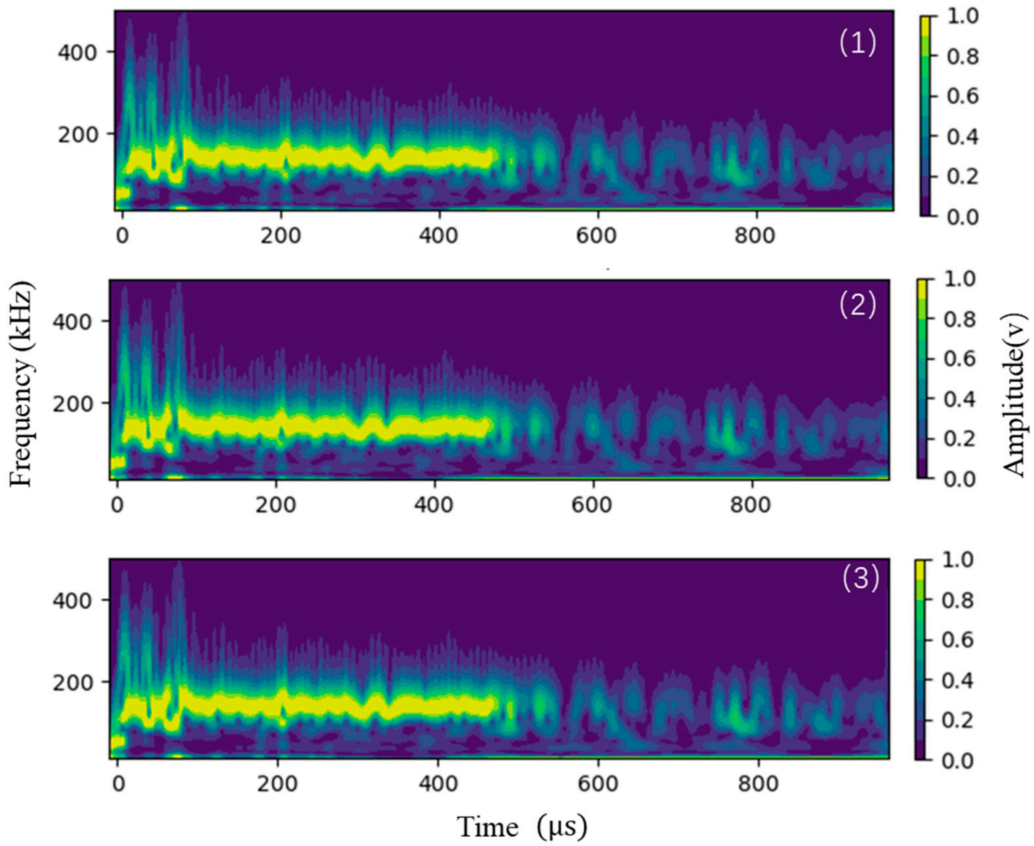

Figure 16. The spectrum analysis results of the receiving waveform. (**1**)–(**3**) are the spectrum diagrams of the received waveforms when the transmitted waveforms are half-cycle sine wave, rectangular wave, and triangular wave respectively.

Table 4. Waveform parameters received with different transmission waveforms.

	Different Transmission Waveforms (1 MHz)		
	Triangular Wave	**Half Sine Wave**	**Rectangular Wave**
Onset time (μs)	23.4	23.33	23.33
Amplitude (mV)	142.52	138.24	145.26
Rise time (μs)	168.33	167.33	168.33

4.4. Influence of Wavelength and Relative Position of the Defect on Received Waveform Parameters

The defect detection accuracy in ultrasonic testing is usually half the wavelength. According to Snell's law, the first arrival wave in the acoustic testing of rock materials travels along the shortest path. If the shortest path does not pass through the defect location, the first arrival data obtained at this time cannot reflect the existence of the defect. Therefore, it is necessary to discuss the influence of the transmitted waveform and the relative position between the straight-line path and the defect on the parameters of the received waveform.

The influence of the emission pulse wavelength changes on the received waveform parameters when monitoring a defect of a specific size was studied. Half-cycle sine waves with frequencies of 200 kHz, 400 kHz, 600 kHz, 800 kHz, and 1 MHz were transmitted with defects on one side of the sample. The waveforms corresponding to different frequency waveforms are shown in Table 5. Then, the waveform was received on the other side of the sample. At the same time, another acoustic-wave-receiving sensor was arranged where the straight-line path of the wave did not pass through the defect to study the influence of whether or not the straight-line path passes through the defect on the received waveform parameters. The straight-line path of the waveform received by the No. 1 sensor passed through the defect, as shown in Figure 12. The straight-line path of the waveform received by the No. 2 sensor did not pass through the defect. The distances from the sound source to sensors No. 1 and No. 2 were 110 mm and 109.66 mm, respectively. The emission waveform is shown in Figure 14. The amplitude was 1 V, and the duration was 0.5 µs. From the surface wave velocity of a complete granite sample (2700 m/s), the wavelengths of different frequency emission waveforms can be obtained as follows.

Table 5. The wavelengths of different frequency waveforms propagating on the surface of the sample.

Frequency (Hz)	200 k	400 k	600 k	800 k	1000 k
Wavelength (mm)	13.5	6.75	4.5	3.34	2.7

The waveforms received by No. 1 and No. 2 sensors with different frequencies are shown in Figure 17.

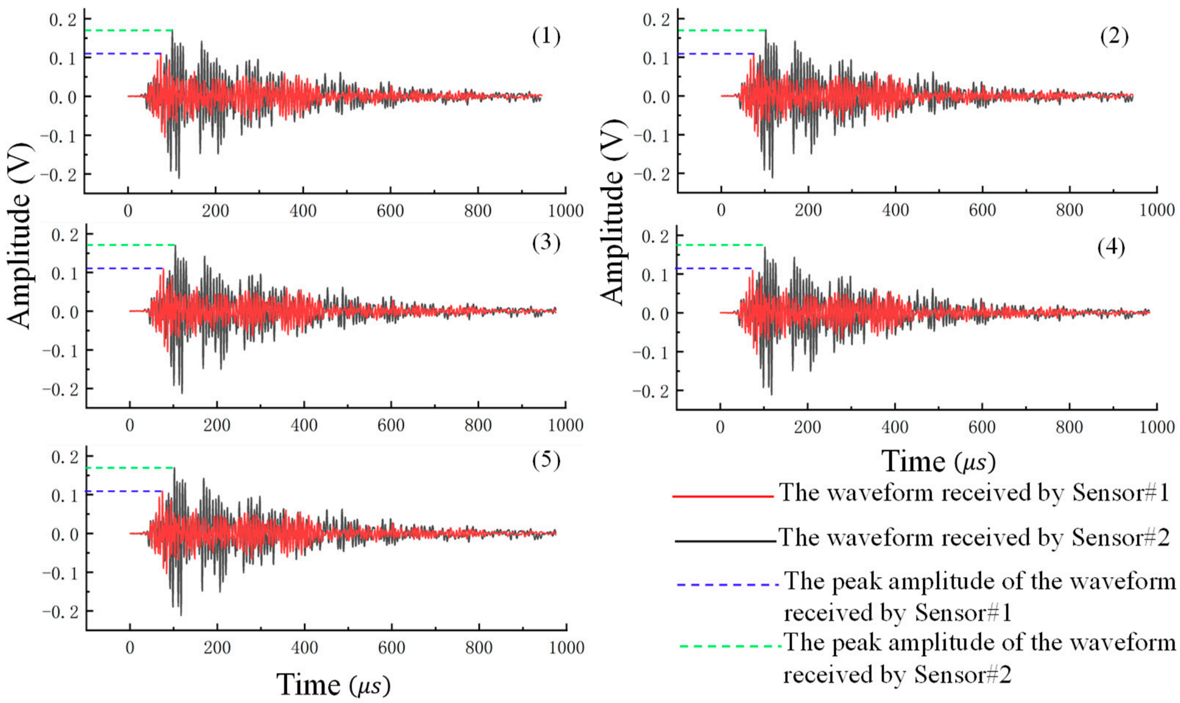

Figure 17. The waveforms received by No. 1 and No. 2 sensors with different frequencies. (**1**) to (**5**) represent the received waveforms when the transmitted waveform frequency is 200 kHz, 400 kHz, 600 kHz, 800 kHz, and 1000 kHz.

The spectrum analysis result of the received waveform is shown in Figure 18. In Figure 18, (1) is the spectrum diagram of the waveform of the straight path passing through the defect, and (2) is the spectrum diagram of the waveform of the straight path not passing through the defect. The start-up time and peak amplitude of the received waveforms are listed in Table 6.

Table 6 reveals that although the distances from sensor 1 and sensor 2 to the sound source were the same, the start-up time of sensor 2 was earlier than that of sensor 1. The amplitude of the waveform received by sensor 2 was much larger than that of sensor 1. The reason for the above phenomenon is a defect 2 mm thick on the straight path from the sound source to sensor 2. The defect led to increased propagation paths and energy attenuation of sound waves.

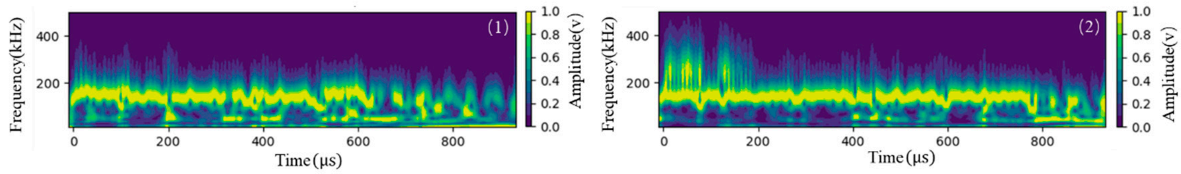

(**a**) The transmitted waveform frequency is 200 kHz.

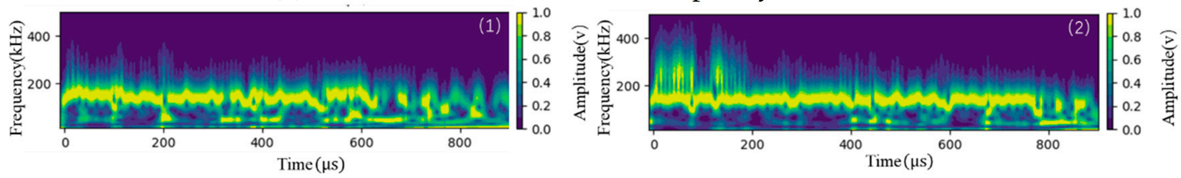

(**b**) The transmitted waveform frequency is 400 kHz.

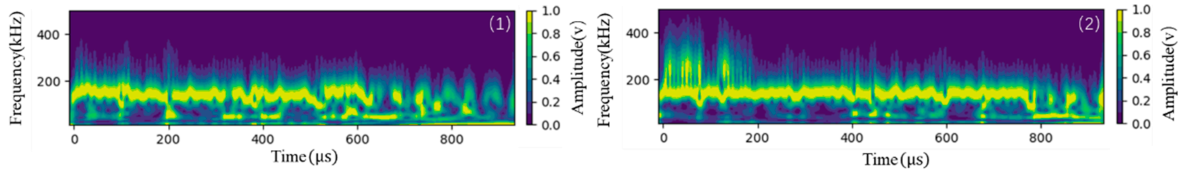

(**c**) The transmitted waveform frequency is 600 kHz.

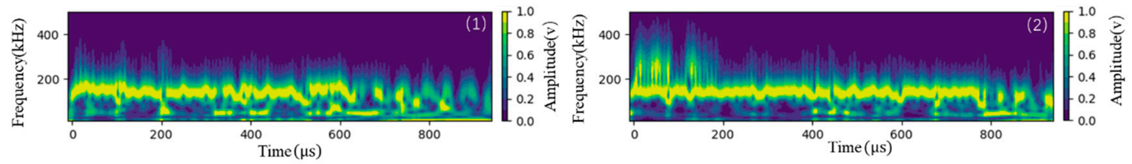

(**d**) The transmitted waveform frequency is 800 kHz.

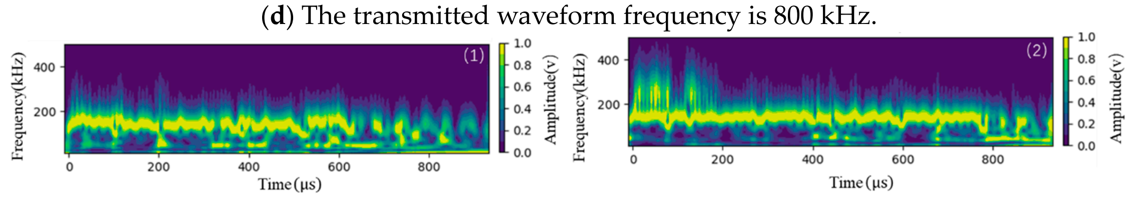

(**e**) The transmitted waveform frequency is 1000 kHz.

Figure 18. The spectrograms of the waves with different source frequencies received by sensor 1 and sensor 2 after propagating in the sample with the defect.

Table 6. The parameters of the waveforms with different source frequencies received by sensor 1 and sensor 2.

	Frequency (Hz)	**200 k**	**400 k**	**600 k**	**800 k**	**1000 k**
Start-up time (μs)	Sensor 1	38.33	38	38.66	40	40
	Sensor 2	37.33	38.33	38.33	38.66	38
Peak amplitude (mv)	Sensor 1	109.8	109.2	110.1	110.1	109.5
	Sensor 2	171.2	170.8	170.2	169.3	169.9

Studies have shown that propagation characteristics of acoustic waves are related to the rocks' mechanical properties in acoustic testing. When the wavelength of the sound wave is much larger than the inhomogeneous scale of the rock sample, the sample can be regarded as a homogeneous medium. Otherwise, it should be considered a heterogeneous medium. From the waveform parameters received by sensor 1 in Tables 5 and 6, it can be seen that when the frequency of the transmitted waveform was greater than 600 kHz, the half wavelength was smaller than the width of the crack, and the travel time of the first wave increased significantly. Therefore, in non-destructive testing of rocks, the sensitivity and accuracy are the best when the half wavelength of the transmitted waveform is equal to half the thickness of the defect to be measured.

5. Conclusions

This paper proposes a new method for solving the wave velocity field by optimizing the fastest path search algorithm. The relationship between the wave velocity field and the damage distribution was established to characterize the damage distribution. The improved method was verified with a granite slab sample during uniaxial compression experiments. The damage characterization results obtained using the proposed method were compared with the results obtained using digital speckle patterns methods, demonstrating the accuracy of the proposed method. Finally, the influence of the transmitted wave's waveform on the test result of the acoustic wave was discussed. The main conclusions are presented as follows:

(1) The improved fastest travel path solution was proposed to obtain an accurate propagation path in layered media and media with defects;

(2) A uniaxial compression experiment with granite flat samples was conducted to verify the accuracy of the improved rock damage distribution characterization method. The results of damage distribution characterization with the proposed method were consistent with the strain rate images obtained by the digital image correlation;

(3) The length and shape of the emitted wave affect the accuracy of results in the rock acoustic wave testing. The half wavelength of the emitted wave should be close to the thickness of the defect being measured. Although shortening the wavelength of the transmitted wave can improve the measurement accuracy, it also increases the wave's attenuation. Using a rectangular or sine wave as the transmitted wave is slightly better than using a triangular wave;

(4) When there are large defects in the medium, diffraction will occur during wave propagation, making it difficult to obtain accurate wave velocity fields at the defects using methods based on first-arrival waves. The method proposed in this manuscript is an improved method based on the first arrival wave travel time and will be subject to this limitation. A possible solution is to improve based on the full waveform and introduce coda waves to expand the time-shifted data to overcome this shortcoming.

Author Contributions: Conceptualization, J.Z. and Y.Z.; methodology, J.Z.; software, Y.Z.; validation, L.L., D.Z. and M.Z.; formal analysis, R.W.; investigation, J.Z.; resources, L.L.; data curation, M.Z.; writing—original draft preparation, J.Z.; writing—review and editing, Y.Z.; visualization, J.Z.; supervision, D.Z.; project administration, Y.Z.; funding acquisition, J.Z. All authors have read and agreed to the published version of the manuscript.

Funding: This research was funded by the National Natural Science Foundation of China grant number [52304152], [52222404], [52074212], and [52004206], by China Postdoctoral Science Foundation Funded Project grant number [2023MD744248] and [2023M732793], by Key Research and Development Program of Shaanxi grant number [2023-LL-QY-07], by Shaanxi Province Technology Innovation Guidance Project grant number [2021QFY04-05], and by Shaanxi Province Postdoctoral Research Project grant number [2023BSHYDZZ156].

Data Availability Statement: Data are contained within the article.

Conflicts of Interest: The authors declare no conflict of interest.

References

1. Gautam, P.K.; Dwivedi, R.; Kumar, A.; Kumar, A.; Verma, A.K.; Singh, K.H.; Singh, T.N. Damage Characteristics of Jalore Granitic Rocks After Thermal Cycling Effect for Nuclear Waste Repository. *Rock Mech. Rock Eng.* **2021**, *54*, 235–254. [CrossRef]
2. Qian, Q.; Zhou, X. Failure Behaviors and Rock Deformation During Excavation of Underground Cavern Group for Jinping I Hydropower Station. *Rock Mech. Rock Eng.* **2018**, *51*, 2639–2651. [CrossRef]
3. Zhao, Y.; Zhao, G.; Xu, L.; Zhou, J.; Huang, X. Mechanical property evolution model of cemented tailings-rock backfill considering strengthening and weakening effects. *Constr. Build. Mater.* **2023**, *377*, 131081. [CrossRef]
4. Zhou, Z.; Cai, X.; Li, X.; Cao, W.; Du, X. Dynamic Response and Energy Evolution of Sandstone Under Coupled Static–Dynamic Compression: Insights from Experimental Study into Deep Rock Engineering Applications. *Rock Mech. Rock Eng.* **2020**, *53*, 1305–1331. [CrossRef]

5. Xie, G.; Liu, L.; Suo, Y.; Zhu, M.; Yang, P.; Sun, W. High-value utilization of modified magnesium slag solid waste and its application as a low-carbon cement admixture. *J. Environ. Manage.* **2024**, *349*, 119551. [CrossRef] [PubMed]
6. Cai, X.; Yuan, J.; Zhou, Z.; Pi, Z.; Tan, L.; Wang, P.; Wang, S.; Wang, S. Effects of hole shape on mechanical behavior and fracturing mechanism of rock: Implications for instability of underground openings. *Tunn. Undergr. Sp. Technol.* **2023**, *141*, 105361. [CrossRef]
7. Guo, Q.; Su, H.; Liu, J.; Yin, Q.; Jing, H.; Yu, L. An experimental study on the fracture behaviors of marble specimens subjected to high temperature treatment. *Eng. Fract. Mech.* **2020**, *225*, 106862. [CrossRef]
8. Fang, Z.; Liu, L.; Zhang, X.; Han, K.; Wang, J.; Zhu, M.; Sun, W.; He, W.; Gao, Y. Carbonation Curing of Modified Magnesium-Coal Based Solid Waste Backfill Material for CO2 Sequestration. *Process Saf. Environ. Prot.* **2023**, *180*, 778–788. [CrossRef]
9. Yin, Q.; Liu, R.; Jing, H.; Su, H.; Yu, L.; He, L. Experimental Study of Nonlinear Flow Behaviors Through Fractured Rock Samples After High-Temperature Exposure. *Rock Mech. Rock Eng.* **2019**, *52*, 2963–2983. [CrossRef]
10. Zhou, Z.; Cai, X.; Cao, W.; Li, X.; Xiong, C. Influence of Water Content on Mechanical Properties of Rock in Both Saturation and Drying Processes. *Rock Mech. Rock Eng.* **2016**, *49*, 3009–3025. [CrossRef]
11. Xie, G.; Suo, Y.; Liu, L.; Yang, P.; Qu, H.; Zhang, C. Pore characteristics of sulfate-activated coal gasification slag cement paste backfill for mining. *Environ. Sci. Pollut. Res.* **2023**, 114920–114935. [CrossRef] [PubMed]
12. Zhou, Z.; Lu, J.; Cai, X.; Rui, Y.; Tan, L. Water saturation effects on mechanical performances and failure characteristics of rock-concrete disc with different interface dip angles. *Constr. Build. Mater.* **2022**, *324*, 126684. [CrossRef]
13. Dai, J.; Liu, J.; Zhou, L.; He, X. Real-Time Ultrasonic Features and Damage Characterization of Deep Shale. *Rock Mech. Rock Eng.* **2023**, *56*, 2535–2550. [CrossRef]
14. Ruan, S.; Liu, L.; Zhu, M.; Shao, C.; Xie, L.; Hou, D. Application of desulfurization gypsum as activator for modified magnesium slag-fly ash cemented paste backfill material. *Sci. Total Environ.* **2023**, *869*, 161631. [CrossRef]
15. Wu, Z.-J.; Wang, Z.-Y.; Fan, L.-F.; Weng, L.; Liu, Q.-S. Micro-failure process and failure mechanism of brittle rock under uniaxial compression using continuous real-time wave velocity measurement. *J. Cent. South Univ.* **2021**, *28*, 556–571. [CrossRef]
16. Zhu, Q.; Li, D.; Li, X.; Han, Z.; Ma, J. Mixed mode fracture parameters and fracture characteristics of diorite using cracked straight through Brazilian disc specimen. *Theor. Appl. Fract. Mech.* **2023**, *123*, 103682. [CrossRef]
17. Zhao, K.; Yang, J.; Yu, X.; Yan, Y.; Zhao, K.; Lai, Y.; Wu, J. Damage evolution process of fiber-reinforced backfill based on acoustic emission three-dimensional localization. *Compos. Struct.* **2023**, *309*, 116723. [CrossRef]
18. Zhang, L.; Zhang, Z.; Chen, Y.; Dai, B.; Wang, B. Crack development and damage patterns under combined dynamic-static loading of parallel double fractured rocks based on DIC technique. *Acta Geotech.* **2023**, *18*, 877–901. [CrossRef]
19. Si, X.; Luo, Y.; Luo, S. Influence of lithology and bedding orientation on failure behavior of "D" shaped tunnel. *Theor. Appl. Fract. Mech.* **2024**, *129*, 104219. [CrossRef]
20. Khoshouei, M.; Bagherpour, R.; Sadeghisorkhani, H.; Jalalian, M.H. A New Look at Hard Rock Abrasivity Evaluation Using Acoustic Emission Technique (AET). *Rock Mech. Rock Eng.* **2022**, *55*, 2425–2443. [CrossRef]
21. Yin, X.C.; Wang, Y.C.; Peng, K.Y.; Bai, Y.L.; Wang, H.T.; Yin, X.F. Development of a new approach to earthquake prediction: Load/unload response ratio (LURR) theory. *Pure Appl. Geophys.* **2000**, *157*, 2365–2383. [CrossRef]
22. Li, X.; Si, G.; Wei, C.; Oh, J.; Canbulat, I. Simulation of ductile fracture propagation using the elastoplastic phase-field damage method calibrated by ultrasonic wave velocity measurement. *Int. J. Rock Mech. Min. Sci.* **2023**, *161*, 105296. [CrossRef]
23. Mei, Y.; Tian, X.; Li, X.; Gepreel, K. Fractal space based dimensionless analysis of the surface settlement induced by the shield tunneling. *Facta Univ. Ser. Mech. Eng.* **2023**, *21*, 737–749.
24. Li, G.; Zhu, C.; He, M.; Zuo, Y.; Gong, F.; Xue, Y.; Feng, G. Intelligent method for parameters optimization of cable in soft rock tunnel base on longitudinal wave velocity. *Tunn. Undergr. Sp. Technol.* **2023**, *133*, 104905. [CrossRef]
25. Weng, L.; Wu, Z.; Wang, Z.; Chu, Z.; Xu, X.; Liu, Q. Acoustic Emission Source Localization in Heterogeneous Rocks with Random Inclusions Using a PRM-Based Wave Velocity Model. *Rock Mech. Rock Eng.* **2023**, *56*, 3301–3315. [CrossRef]
26. Jiang, G.; Zuo, J.; Li, Y.; Wei, X. Experimental Investigation on Mechanical and Acoustic Parameters of Different Depth Shale Under the Effect of Confining Pressure. *Rock Mech. Rock Eng.* **2019**, *52*, 4273–4286. [CrossRef]
27. D'Angiò, D.; Lenti, L.; Martino, S. Microseismic monitoring to assess rock mass damaging through a novel damping ratio-based approach. *Int. J. Rock Mech. Min. Sci.* **2021**, *146*, 1–9. [CrossRef]
28. Zhao, Y.; Yang, T.; Zhang, P.; Zhou, J.; Yu, Q.; Deng, W. The analysis of rock damage process based on the microseismic monitoring and numerical simulations. *Tunn. Undergr. Sp. Technol.* **2017**, *69*, 1–17. [CrossRef]
29. Madhubabu, N.; Singh, P.K.; Kainthola, A.; Mahanta, B.; Tripathy, A.; Singh, T.N. Prediction of compressive strength and elastic modulus of carbonate rocks. *Measurement* **2016**, *88*, 202–213. [CrossRef]
30. Chen, H.; Zhang, G.; Fan, D.; Fang, L.; Huang, L. Nonlinear Lamb wave analysis for microdefect identification in mechanical structural health assessment. *Meas. J. Int. Meas. Confed.* **2020**, *164*, 108026. [CrossRef]
31. Umrao, R.K.; Sharma, L.K.; Singh, R.; Singh, T.N. Determination of strength and modulus of elasticity of heterogenous sedimentary rocks: An ANFIS predictive technique. *Measurement* **2018**, *126*, 194–201. [CrossRef]
32. Abbas, H.A.; Mohamed, Z.; Abdul Kudus, S. Deformation behaviour, crack initiation and crack damage of weathered composite sandstone-shale by using the ultrasonic wave and the acoustic emission under uniaxial compressive stress. *Int. J. Rock Mech. Min. Sci.* **2023**, *170*, 105497. [CrossRef]

33. Rodríguez, P.; Celestino, T.B. Assessment of damage distribution in brittle materials by application of an improved algorithm for three-dimensional localization of acoustic emission sources with P-wave velocity calculation. *Constr. Build. Mater.* **2020**, *231*, 117086. [CrossRef]
34. Liu, B.; Wang, J.; Yang, S.; Xu, X.; Ren, Y. Forward prediction for tunnel geology and classification of surrounding rock based on seismic wave velocity layered tomography. *J. Rock Mech. Geotech. Eng.* **2023**, *15*, 179–190. [CrossRef]
35. Zhang, Y.-B.; Yao, X.-L.; Liang, P.; Wang, K.-X.; Sun, L.; Tian, B.-Z.; Liu, X.-X.; Wang, S.-Y. Fracture evolution and localization effect of damage in rock based on wave velocity imaging technology. *J. Cent. South Univ.* **2021**, *28*, 2752–2769. [CrossRef]
36. Heimann, S.; Vasyura-Bathke, H.; Sudhaus, H.; Isken, M.P.; Kriegerowski, M.; Steinberg, A.; Dahm, T. A Python framework for efficient use of pre-computed Green's functions in seismological and other physical forward and inverse source problems. *Solid Earth* **2019**, *10*, 1921–1935. [CrossRef]
37. Liu, Y.; Hong, X.; Zhang, B. A novel velocity anisotropy probability imaging method using ultrasonic guided waves for composite plates. *Measurement* **2020**, *166*, 108087. [CrossRef]
38. Ivansson, S. Seismic borehole tomography—Theory and computational methods. *Proc. IEEE* **1986**, *74*, 328–338. [CrossRef]
39. Gorbatov, A.; Dominguez, J.; Suarez, G.; Kostoglodov, V.; Zhao, D.; Gordeev, E. Tomographic imaging of the P-wave velocity structure beneath the Kamchatka peninsula. *Geophys. J. Int.* **1999**, *137*, 269–279. [CrossRef]
40. Goodfellow, S.D.; Tisato, N.; Ghofranitabari, M.; Nasseri, M.H.B.; Young, R.P. Attenuation Properties of Fontainebleau Sandstone During True-Triaxial Deformation using Active and Passive Ultrasonics. *Rock Mech. Rock Eng.* **2015**, *48*, 2551–2566. [CrossRef]
41. Xu, C.; Peng, L.; Deng, M. Phased array imaging for damage localization using multi-narrowband Lamb waves. *Mech. Syst. Signal Process.* **2023**, *190*, 110134. [CrossRef]
42. Dines, K.A.; Lytle, R.J. Computerized geophysical tomography. *Proc. IEEE* **1979**, *67*, 1065–1073. [CrossRef]
43. Kim, B.; Chen, J.; Kim, J. International Journal of Rock Mechanics and Mining Sciences Relation between crack density and acoustic nonlinearity in thermally damaged sandstone. *Int. J. Rock Mech. Min. Sci.* **2020**, *125*, 104171. [CrossRef]
44. Shirole, D.; Hedayat, A.; Ghazanfari, E.; Walton, G. Evaluation of an Ultrasonic Method for Damage Characterization of Brittle Rocks. *Rock Mech. Rock Eng.* **2020**, *53*, 2077–2094. [CrossRef]
45. Zhou, Z.; Rui, Y.; Cai, X.; Lu, J. Constrained total least squares method using TDOA measurements for jointly estimating acoustic emission source and wave velocity. *Meas. J. Int. Meas. Confed.* **2021**, *182*, 109758. [CrossRef]
46. Yang, J.; Dai, J.; Yao, C.; Jiang, S.; Zhou, C.; Jiang, Q. Estimation of rock mass properties in excavation damage zones of rock slopes based on the Hoek-Brown criterion and acoustic testing. *Int. J. Rock Mech. Min. Sci.* **2020**, *126*, 104192. [CrossRef]